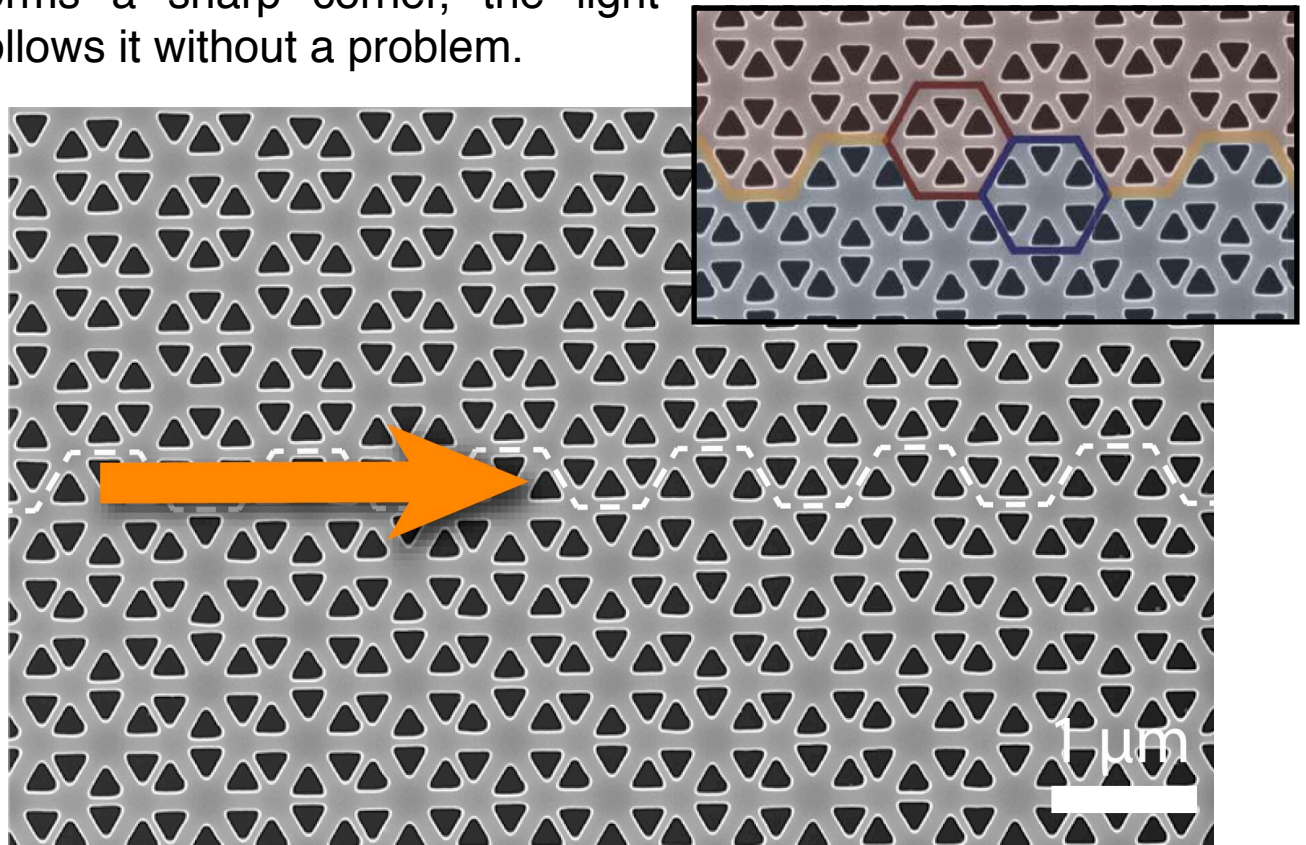The material, a photonic crystal, consists of two parts that each have a slightly different pattern of perforations. Light can propagate along the boundary between these two parts in a special way: It is "topologically protected," and therefore does not bounce back at imperfections. Even when the boundary forms a sharp corner, the light follows it without a problem.



The perforated slab of silicon. The top and bottom crystal structures differ slightly; along the boundary between two parts (dotted line) light can be guided.

For these light waves the polarization of light rotates in a certain direction, analogous to the spin of electrons in topological insulators. The polarisation of light determines the direction in which this light propagates. Because polarization cannot easily change, the light wave can even flow around sharp corners without reflecting or getting scattered, as would happen in a regular waveguide.

# Direct observation of topological edge states in silicon photonic crystals: Spin, dispersion, and chiral routing

Nikhil Parappurath[1], Filippo Alpeggiani[2], L. Kuipers[2], Ewold Verhagen[1]*

Topological protection in photonics offers new prospects for guiding and manipulating classical and quantum information. The mechanism of spin-orbit coupling promises the emergence of edge states that are helical, exhibiting unidirectional propagation that is topologically protected against back scattering. We directly observe the topological states of a photonic analog of electronic materials exhibiting the quantum spin Hall effect, living at the interface between two silicon photonic crystals with different topological order. Through the far-field radiation that is inherent to the states' existence, we characterize their properties, including linear dispersion and low loss. We find that the edge state pseudospin is encoded in unique circular far-field polarization and linked to unidirectional propagation, thus revealing a signature of the underlying photonic spin-orbit coupling. We use this connection to selectively excite different edge states with polarized light and directly visualize their routing along sharp chiral waveguide junctions.

## INTRODUCTION

The concept of topology has proven immensely powerful in physics, describing new phases of matter with unique properties. The connection of the quantum Hall effect to band structure topology explained the emergence of topologically protected unidirectional transport of electrons. These states exist at the edge of two-dimensional systems subject to an external magnetic field that breaks time-reversal (TR) symmetry. The prediction (1) and observation (2, 3) of the quantum spin Hall effect (QSHE) unlocked a new door in the field of topological physics. This effect relies on spin-orbit coupling instead of an external magnetic field, causing spin-up and -down electrons to propagate in opposite directions in states that are protected by TR symmetry. There has been a recent surge in attempts to implement topological protection in the acoustic, mechanical, microwave, and optical domains (4–17), owing to the application potential of robust transport. A particular opportunity is provided by photonic spin-orbit coupling (18, 19). Photonic analogs of QSHE were realized using arrayed ring resonators, where the helicity of propagation in the ring takes the role of (pseudo)spin (20–23). Crystal symmetry is known to provide routes toward topological band structures (24). Recently, the QSHE was predicted to occur in photonic crystals with special symmetries, with edge-state propagation direction linked to local circular Poynting vector flows (25–27). Such states were realized in the microwave domain (28, 29) and coupled to spin-polarized quantum dots (30). Creating topological photonic states in the telecom domain is especially promising in view of exciting possibilities such as nanoscale routing, resilience to disorder, one-way transport, and robust light emission in integrated photonic chips. In light of these, the manipulation and imaging of single edge states, quantification of their losses and their topological protection, and study of traits that are unique to these states are all important pursuits. In contrast to valley Hall topological photonic crystals (31–33) that operate below the light line, topological photonic crystals using QSHE offer the possibility to access their properties via far-field radiation (34).

Here, we directly observe topological photonic states at telecom wavelengths in photonic crystals in silicon-on-insulator technology. Through angular spectroscopy and polarimetry, we retrieve the intriguing properties of single edge states that appear at the interfaces between crystals with different topological order. We reveal that the radiation of the topological states carries their unique nature: The states' pseudospin is encoded in the circular polarization of their far field, and one-to-one related to the unidirectional propagation (Fig. 1A). Through this connection, we selectively excite modes in opposite directions and map their propagation in real space. We determine their dispersion and loss and show that the measured propagation quality factors of ~450 are intrinsically limited by the very radiation we observe. Moreover, we experimentally observe an anticrossing between unidirectional modes due to symmetry breaking at the crystal edge for the first time. A tight-binding model fitted to the measured bulk-state dispersion correctly predicts the magnitude of this spin-spin scattering. Last, we show through direct imaging how the pseudospin in combination with a chiral waveguide crossing can be used to effectively route optical information in compact footprints.

As photonic systems do not feature the Kramers doubling that guarantees the existence of electronic states of opposite spin in crystals, we follow a symmetry-based approach to topological photonics outlined by Wu and Hu (25) and Barik et al. (26). The scheme starts from a photonic crystal with scattering sites arranged in a honeycomb lattice. Viewing such crystals as a triangular lattice of hexagonal unit cells with six sites each, they exhibit a doubly degenerate Dirac cone at the $\Gamma$ point. We fabricate photonic crystals with hexagonal unit cells containing equilateral triangular holes in a silicon membrane through electron beam lithography and reactive ion and wet etching of a silicon-on-insulator substrate. Figure 1B shows a pseudocolored scanning electron micrograph in top view. Preserving the $C_6$ crystal symmetry, each hexagonal cluster is deformed either by concentrically shifting the holes inward ("shrunken lattice"; Fig. 1B, top) or outward ("expanded lattice"; Fig. 1B, bottom), without altering unit cell size. Such deformations open a gap at the Dirac point but qualitatively in different ways. A continuous deformation of the lattice from shrunken to expanded is necessarily accompanied by a closing of the bandgap, akin to the behavior in a one-dimensional Su-Schrieffer-Heeger model
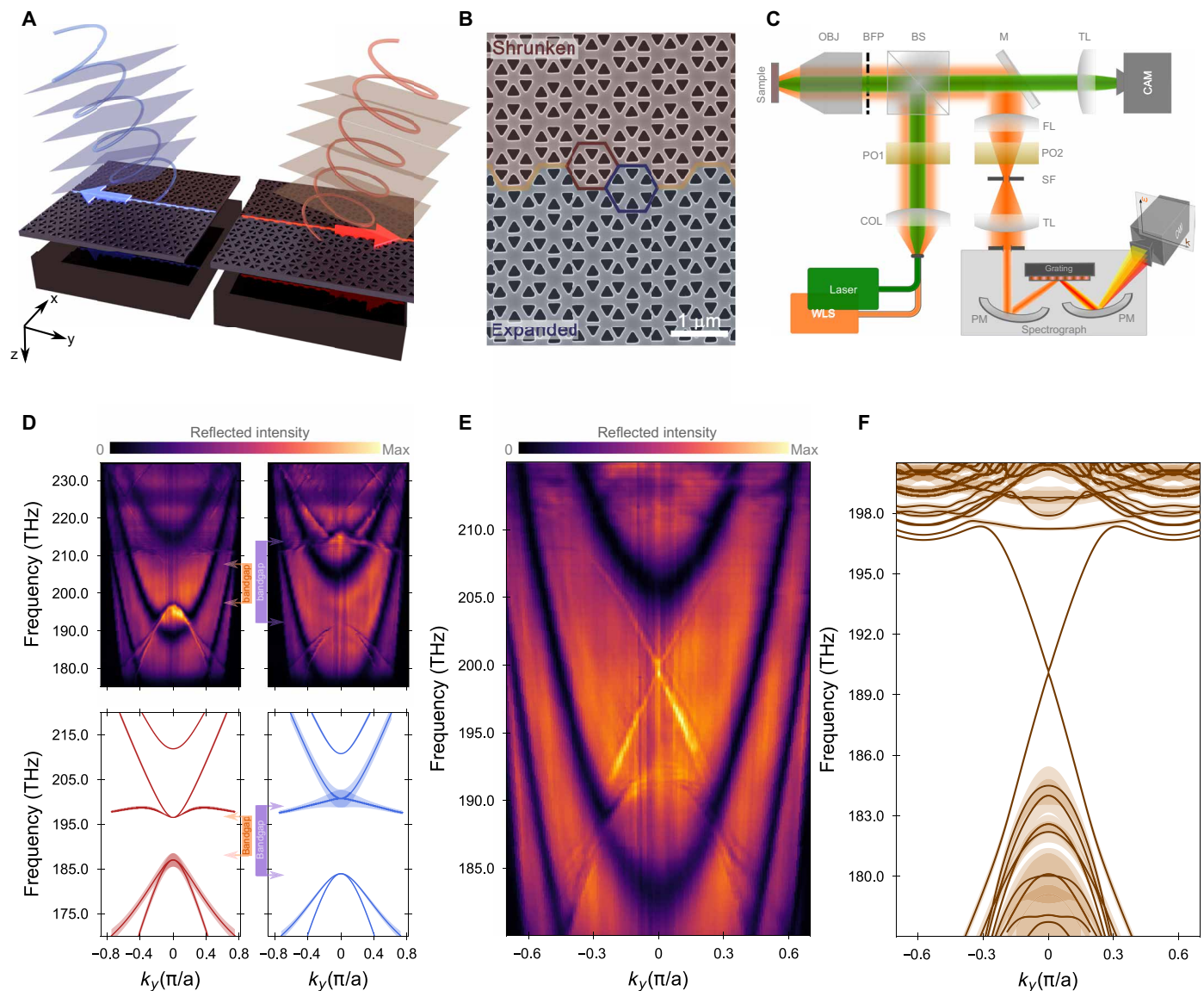
[1]Center for Nanophotonics, AMOLF, Science Park 104, 1098 XG Amsterdam, Netherlands. [2]Department of Quantum Nanoscience, Kavli Institute of Nanoscience, Delft University of Technology, 2600 GA Delft, Netherlands.
*Corresponding author. Email: verhagen@amolf.nl

**Fig. 1. Spectroscopy of topological edge states.** (**A**) Spin-orbit coupling in topological photonic crystals: Chirality of the radiation field is connected to propagation direction of topological photonic crystal edge states. (**B**) A scanning electron micrograph of the fabricated sample. The yellow line represents the arm-chair edge between two pseudocolored regions of differing topology. Red and blue hexagons highlight the respective unit cells. (**C**) Schematic diagram of the experimental setup. In the Fourier-space spectroscopy mode (orange path), the back-focal plane (BFP) is imaged onto the spectrometer slit. A spatial filter (SF) chooses the area from which light is collected. Quarter-wave plates (QWPs) and polarizers define input polarization (PO1) and allow polarimetry of reflected light (PO2). In the real-space imaging mode (green path), the sample plane is imaged onto the camera without SF. See Materials and Methods for details and abbreviations. (**D**) Measured (top) and calculated (bottom) dispersion of shrunken (left) and expanded (right) lattices for diagonally polarized incidence. The measured reflection intensity is normalized to the maximum pixel value among the images. Linewidths of the calculated modes, scaled up five times, are shown as shaded regions in the bottom panels. (**E** and **F**). Measured and calculated dispersion of the edge states. Calculated linewidths are shown as a shaded region in (F).

(9, 35, 36). The shrunken and expanded lattices are then associated with two different band structure topologies analogous to a $\mathbb{Z}_2$ topological insulator. A band inversion takes place across the closing of the gap, meaning that the nature of the states at the top and bottom band edges is opposite for shrunken and expanded crystals. The states of the bottom (top) bands in the shrunken (expanded) lattice, characterized by the out-of-plane magnetic field $H_z$, resemble $p$-orbitals, whereas the top (bottom) bands are $d$-like (25, 26). Bulk-edge correspondence guarantees the existence of topologically protected states at the edge of two domains of different topology, such as the arm-chair interface in Fig. 1B.

The deformation of the unit cell that opens the band gap also couples the TE-like states in the silicon slab to far-field radiation. As both the band edges and edge states appear close to the Γ point, they are naturally phase-matched to free-space radiation. In either expanded or shrunken lattices, the fundamental Bloch harmonic of the photonic crystal eigenmodes can carry finite weight. Gorlach *et al.* have shown how this radiation can be used to study the collective properties of

bulk crystals and arrays of alternating strips of expanded and shrunken lattices in nanoparticle metasurfaces (*34*). Building on these principles, we use the radiation to observe and characterize topological states on single edges between crystal domains. This allows us to not only map their energy and momentum but also study their polarization and image their localization and propagation.

## RESULTS AND DISCUSSION
### Bulk- and edge-state dispersion
We use the reflectometry setup outlined in Fig. 1C to directly measure the photonic crystal band dispersion in reciprocal space. Focused, broadband incident light excites the crystal modes. Directly reflected and reradiated light is collected from an area of $\sim 30 \times 102$ μm, restricted by a spatial filter (see Materials and Methods). By imaging the objective back focal plane onto the entrance slit of a spectrograph (*37*), we record two-dimensional images of frequency versus $k_y$ wave vector of reflected light with $k_x = 0$ on an infrared (IR) camera at the spectrograph output.

The top panels in Fig. 1D show the measured reflection as a function of frequency and $k_y$ from shrunken and expanded lattice crystals for diagonally polarized input. The spectrally broad fringes are due to Fabry-Pérot-like reflections between the suspended membrane and the substrate (see fig. S1). We observe sharper resonant features interfering with this direct reflection background to produce bands with Fano lineshapes. The dispersion of these states corresponds well to the calculated photonic crystal band diagrams in the bottom of Fig. 1D for both lattices, apart from an overall ~10-THz frequency offset that is likely related to deviations of fabricated hole size and shape from designed geometry. Bandgaps are visible around optical frequencies of ~200 THz, with widths of 9 THz ($\Delta\omega/\omega_0 \approx$ 4.4%) for the shrunken lattice and 18 THz ($\Delta\omega/\omega_0 \approx 8.9\%$) for the expanded lattice. These measured bandgaps are in good agreement with the calculated relative gaps of 4.7 and 7.8%, respectively.

Figure 1D shows the band inversion between shrunken and expanded lattice reflection, manifested in the leakiness of their upper and lower bands (*34*). The $p$-orbitals of $H_z$ associated with the bottom (top) band edge of the shrunken (expanded) lattice mean that their in-plane electric field distributions are even with respect to the center of the unit cell. As such, these states can couple to radiation that is normal to the slab, whereas the $d$-orbital states are quadrupolar and dark. We observe the bright spectral features of the $p$-orbital states at opposite sides of the gap for the two lattices, accompanied by linewidth reduction of the other edge. The latter is confirmed by the mode calculations in the bottom panels of Fig. 1D, where the shading widths are proportional to the imaginary part of the eigenmode frequency. These radiation properties thus confirm that the two lattices feature bandgaps of different topological character.

Figure 1E shows the band diagram measured in reflection when exciting the armchair-like edge between regions of expanded and shrunken lattices with a diagonally polarized focused beam. The focused excitation allows the study of states that are excited locally, while the spatial filter is chosen such as to maximize the signal-to-background ratio of single edge states while retaining good angular resolution. We observe two states that close the bandgap with opposite velocities, crossing at the Γ point. They exhibit the characteristic linear dispersion of edge states in QSHE topological insulators, with a measured group velocity that does not vary much ($\sim c/6.3$ to $\sim c/5.3$) over the effective band gap. The measured band diagrams correspond well to the calculated modes, shown in Fig. 1F.

## Detecting pseudospin
We then turn to study the polarization properties of these edge states, modifying the setup to add the functionality of polarimetry. This allows quantifying the polarization of the reflected field in terms of its Stokes parameters (*38*). We first excite the edge with circularly polarized (CP) light of different handedness and plot the intensity of the polarized component of the reflected field, $I_P = \sqrt{S_1'^2 + S_2'^2 + S_3'^2}$, where $S_i$ are unnormalized Stokes parameters, in Fig. 2 (A and B). One recognizes that the two edge states of positive or negative group velocity are excited selectively with near-perfect contrast using either left or right CP inputs, respectively. This selective behavior is independent of the exact position of the excitation spot (see the section 'Imaging propagation and topological routing' below), indicating that the far-field helicity probes a global property of the edge states.

This observed unique helical nature of the edge states' far field can be understood by considering how these states originate from the $p$- and $d$-like orbitals in the infinite lattice unit cells. At the Γ point, the bands are degenerate. In the $H_z$ field basis of $|p_\pm\rangle = (|p_x\rangle \pm i|p_y\rangle)/\sqrt{2}$ and $|d_\pm\rangle = (|d_{(x^2-y^2)}\rangle \pm i|d_{(xy)}\rangle)/\sqrt{2}$, a tight-binding model that describes coupling between the sites results in a $4 \times 4$ Hamiltonian
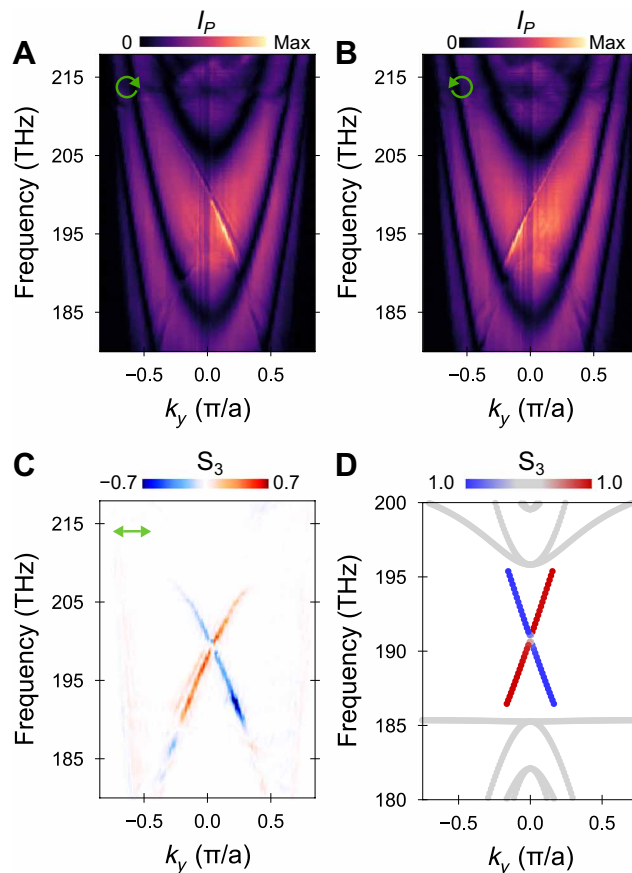


**Fig. 2. Polarimetry results.** (**A** and **B**) Total reflected intensity of the polarized field ($I_P$) as a function of frequency and wave vector $k_y$ when the edge is excited with right (**A**) and left (**B**) CP light. Images are normalized with respect to corresponding maximum pixel values. (**C**) Measured circular polarization intensity (normalized Stokes parameter $S_3$) when the edge is excited with light that is linearly polarized along $y$. A center block is placed at the real-space plane to spatially filter background reflections (see Materials and Methods). (**D**) Normalized $S_3$ for the edge states as predicted by the tight-binding model.

in the approximation of nearest-neighbor coupling and linear expansion in $k_x$ and $k_y$ that is block-diagonal, meaning that only states of the same pseudospin ± are coupled (25). As a result, the edge states that connect the top and bottom bands must be associated with a single pseudospin, admixing either $|p_+\rangle$ and $|d_+\rangle$ or $|p_-\rangle$ and $|d_-\rangle$. Whereas the full edge state field near the nanostructured photonic crystal is generally complex and composed of multiple orbitals, it is the $p$-like component that is predominantly responsible for the plane wave emitted to the far field. Thus, we find that the fundamental harmonic of the Bloch mode must be CP, with handedness equal to the pseudospin.

We can quantify this radiation and its polarization in the tight-binding model by calculating the total in-plane dipole moment inside the unit cell $\boldsymbol{p} \propto \sum_{i=1}^{6} \hat{\theta}_i \psi_i$, where $\hat{\theta}_i$ is the azimuthal unit vector of the $i$th site and $|\psi\rangle$ is a six-dimensional scalar "wave function" with components $\psi_i$ corresponding to $H_z$ at site $i$. To also correctly predict the polarization of the bulk bands, we need to extend the tight-binding model beyond the nearest-neighbor approximation, which predicts degenerate bulk bands over the entire reciprocal space (26). In contrast, we observe splitting of both upper and lower bands away from the Γ point in experiment and finite element simulation, with linear polarization (see fig. S2). By introducing additional coupling terms up to third order in the tight-binding model (see fig. S3), we retrieve the observed lifting of degeneracy, allowing the prediction of the polarization of each observed state.

To assess the polarization of the edge and bulk states experimentally, we excite the edge with light that is horizontally polarized and perform full polarization tomography of the emitted radiation as a function of frequency and wave vector along the edge. To isolate the fields of the photonic crystal modes, the spatial filter is modified to block direct reflection from the slab and the substrate below (see Materials and Methods). Figure 2C displays the measured Stokes parameter $S_3$—which quantifies the detected CP intensity—normalized to the maximum value of total intensity of the polarized component. We see that only the edge states exhibit a substantial degree of CP. Their opposing helicity is evident: The emission of the negative pseudospin state with negative group velocity is mostly left CP and that of the positive pseudospin state with positive group velocity is mostly right CP. In other words, we directly observe the pseudospin of the topological edge states, and the experiments reveal a clear signature of the photonic spin-orbit coupling that lies at the root of the QSHE.

## Symmetry breaking and spin-spin scattering

The measured far-field polarization is in good agreement with the results of the tight-binding model, of which the parameters are fitted to the observed frequencies. We find that, also with the inclusion of the higher-order coupling terms, the average dipole moment remains CP. This behavior is illustrated in Fig. 2D, which shows the Stokes parameter $S_3$ calculated by our theoretical model for edge and bulk modes.

The inclusion of higher-order coupling terms leads to the prediction of a small anticrossing between the two edge states, as can be seen in Fig. 2D. Topological protection in these systems is linked to a "pseudo" TR symmetry, which needs the preservation of $C_6$ symmetry while deforming the honeycomb lattice unit cells (39). However, at the interface between two deformed lattices, $C_6$ symmetry breaking is unavoidable. This results in photonic spin-spin scattering—coupling of the counter-propagating edge states that opens a small gap around the Γ point (40). We see this also in experiment as a discontinuity around 200 THz in Fig. 2 (A and B). The amount of spin-

spin scattering and thus the intrinsic limit to topological protection in photonic crystals can be recognized from this gap.

Figure 3A shows reflected intensity normalized to that from a silver mirror around the Γ point for horizontally polarized input, showing the anticrossing. The reflectance at $k_y = 0$ (Fig. 3B) is fitted with two complex Lorentzians together with a slowly varying background (see Materials and Methods). The edge states are split by a 1.0-THz gap. This compares well to the 0.6-THz gap predicted by the beyond–nearest-neighbor tight-binding model, of which the parameters were obtained from fitting to bulk simulation data, independently of the gap. We observed a similar gap of 1.2 THz on a zigzag edge. The finite element simulations themselves also predict splitting of the states at the Γ point for both types of edges, as shown in Fig. 3B. We do note that the bandgap predicted by the finite element calculations was somewhat smaller (∼0.1 THz) for the armchair edge. As any realistic photonic crystal sample features finite structural disorder and deviations from design, some of these imperfections (which break $C_6$ symmetry) may lead to spin-spin scattering in addition to the intrinsic coupling expected in the "perfect" structures assumed by the tight-binding and finite element calculations. Given the values we report here from experiments and both types of theoretical calculation, we conclude that it is likely that intrinsic spin-spin coupling contributes substantially to the observed gaps. Further studies that systematically vary in design and disorder should determine whether spin-spin scattering is practically limited by fundamental symmetry breaking at the interface or by other factors and to which extent it can be mitigated. We showed here that Fourier spectroscopy provides an effective method to probe even small amounts of scattering and investigate the limits to topological protection and spin-orbit coupling in photonics.

We also quantify the edge-state losses from the reflectance fit. Shaded regions in Fig. 3B depict the fitted linewidths of the modes, which exhibit quality factors ($Q$) of 413 and 486. These deviate not far from the $Q \approx 604$ predicted by finite element method (FEM) simulation. The difference could be due to structural disorder, deviation of hole shape with respect to the designed (simulated) structure, or interaction of the propagating mode with radiation fields reflected from the Si substrate. Nonetheless, we conclude that the edge states propagate over distances of many wavelengths in the photonic crystal slab, even though their fundamental Bloch component is inherently
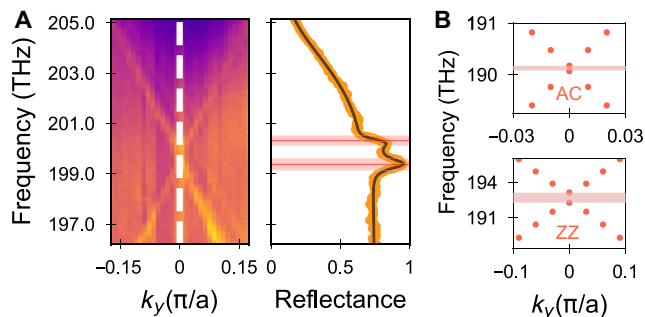


**Fig. 3. Quantifying spin-spin scattering in the system.** (**A**) Measured reflectance (left panel) showing dispersion of edge states as a function of wave vector $k_y$ and measured intensity (right panel) along the cross-cut indicated by the white line in the left panel (orange data). The black line shows a fit with a set of complex Lorentzians (see Materials and Methods). Red lines and shaded areas correspond to the extracted resonance frequencies and linewidths. (**B**) Splitting (red shaded region) of armchair (top) and zigzag (bottom) edge states obtained from finite element simulations.

phase-matched to the free-space continuum. We expect radiation losses, as well as spin-spin scattering, to reduce further for smaller deformation of the shrunken and expanded unit cells. However, since that would simultaneously reduce bandgap width and increase transverse mode extent, it would be interesting to explore how other strategies, including design of microscopic structure, allow minimization of loss and backscattering.

## Imaging propagation and topological routing

The radiation field also enables mapping edge state propagation in real space (Fig. 4), upon locally and selectively exciting them with polarized light. Figure 4 (B to D) shows images taken with an IR camera using the green beam path in Fig. 1C, when polarized laser light at 1512 nm is focused at the edge. We observe the topological edge states, propagating out of the excitation focus along the edges between the two lattices. They decay over distances of tens of micrometers, in accordance with the measured linewidths. As Fig. 4 (B to D) shows, left (right) CP light excites only the positive (negative) pseudospin mode, which propagates only in the downward (upward) direction. When the edge is excited with vertically polarized light, propagation has equal preference for each direction.

To show that the directivity is independent of the position of the laser focus, we scan the excitation spot across the armchair edge by moving the sample in the horizontal direction and plot the difference $\Delta I$ between the edge-state intensities launched to the top and to the bottom in Fig. 4E. These intensities $I_U$ and $I_D$ are obtained by integrating the detected intensity in image regions that correspond to edge states launched "up" ($U$) or "down" ($D$) from the excitation spot, as shown in Fig. 4F. Figure 4E depicts $\Delta I = I_U - I_D$ for both circular polarization handedness "$L$" and "$R$." The constant offset to the differential intensity ($\sim 0.4$ on this scale) is due to a spatially varying background intensity. The excitation probability for both polarizations peaks at the position marked "0," with smaller sidelobes that must be related to the spatial overlap of the laser beam and the edge state. We note that the direction into which topological edge states are launched (up or down) does not depend on the exci-

tation spot position but only on the incident polarization, as either differential intensity only deviates from the background value in a single direction. Thus, the spin-orbit coupling as evidenced in the far field is independent of the position in the mode field, in contrast to the spin-orbit coupling that leads to preferential emission directions for spin-polarized quantum dots (30). The difference can be related to the fact that the emitters act as near-field point sources, which couple not only to the fundamental Bloch harmonic of the edge-state field. Here, our experiments probe the global pseudospin of either of the edge states.

Last, we study the routing of topological edge states at sharp corners formed by a junction between an armchair and a zigzag edge that separate four distinct photonic crystal regions, as depicted in Fig. 5A. The edges form a total of four topological waveguides emanating from the junction, of two different classes: For positive pseudospin, the two vertical edges support propagation toward the junction, whereas the horizontal edges allow propagation away from the junction. For negative pseudospin, the directions are reversed.

Figure 5 (B to D) shows images taken for various excitation points on the vertical edge marked in Fig. 5A. We can see in Fig. 5B that the positive pseudospin edge state excited with left CP at position 1 propagates downward toward the junction, but not further, as propagation in the bottom waveguide is forbidden for this pseudospin. Had the junction been perfectly symmetric, this pseudospin could have propagated in both the left and right horizontal waveguides. However, the light appears to propagate only into the right waveguide. This is even more clear when the state is excited at position 2, only a few micrometers from the junction (Fig. 5C). The pronounced observed preference for taking a turn to the right waveguide must be related to the microscopic structural asymmetry of the junction, visible in the inset of Fig. 5A. The junction exhibits a chiral character, where we can recognize two continuous interfaces between the expanded and shrunken lattice unit cells that do not cross. The light is efficiently routed along the interface that connects the top and right waveguides, even though it is separated from the other interface by subunit cell distance—much smaller than the transverse extent of the
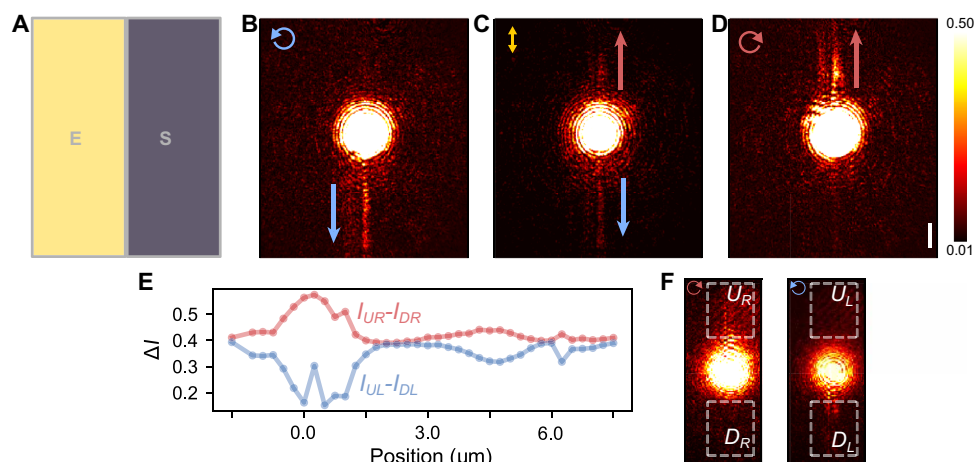


**Fig. 4. Real-space images of edge state propagation.** (**A**) A schematic diagram showing the edge between expanded (E) and shrunken (S) lattices where a focused single wavelength laser excites the sample. (**B** to **D**) Real-space camera images when the incident light is left circularly, linearly, and right CP, respectively. Images are normalized to the maximum pixel value among the three. Scale bar, 10 μm. (**E**) Transverse dependence of excitation, showing that selectivity is independent of excitation position. The plotted value $\Delta I$ shows the difference between integrated intensities in two areas $U$ and $D$ as defined in each panel of (**F**), when a right (red) and a left CP (blue) excitation spot is moved across an armchair edge. The excitation position at 0 μm corresponds to an approximate center of the waveguide. (F) Images recorded for the excitation position 0 μm. The dashed rectangles correspond to the areas under which the intensity is integrated in (E).
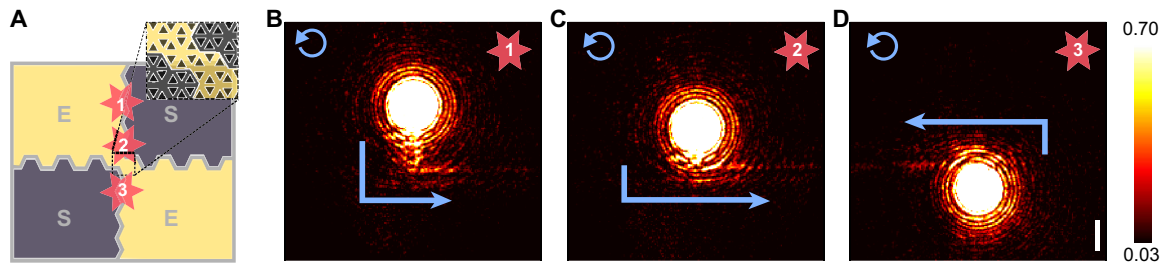
**Fig. 5. Routing of light around a topologically protected chiral junction.** (**A**) A schematic diagram showing a junction formed by four topological edges. Inset shows a zoomed-in image of the chiral junction. Real-space images (**B** to **D**) show light propagation when the sample is excited by a left CP monochromatic laser at positions 1, 2, and 3 marked in (A). All three images (B to D) are normalized to the maximum pixel value among the three. Scale bar, 10 μm.

modes. In a control experiment (Fig. 5D), we see that the same pseudo-spin excited in the bottom waveguide follows the other interface, into the left waveguide. We also observe neither back-reflection nor an enhancement of out-of-plane scattering at the junction. Together, these observations suggest the important role of spin-momentum locking in the routing of the edge states, allowing them to take sharp corners and protect them from scattering to other modes.

## Conclusions

To conclude, we have directly excited and observed topologically protected edge states at telecom wavelengths in a silicon photonic platform. We characterized the propagation, loss, dispersion, and routing along sharp corners of single edge states. We demonstrated that the pseudospin of the states is inherently encoded in the circular polarization of their far fields and used this strong spin-orbit coupling to selectively excite the topological states with a focused laser beam. The used Fourier spectroscopy technique makes it possible to quantify the inherent spin-spin scattering of the system, opening doors to further understand and control topological protection in QSHE systems, as well as the connections between chirality and topology (41). This work directly enables the development of novel photonic topological systems for a wide variety of applications. These include components for integrated photonic chips, as well as application that could leverage the polarized free-space radiation that is intrinsic to these types of edge states, including chiral quantum optical interfaces, enantiomeric sensing, and lasing at the nanoscale.

## MATERIALS AND METHODS
### Experimental design

This work aimed to observe and study the properties of topological states in silicon photonic crystals. Sample design was assisted by numerical simulations, and samples were fabricated using lithographic nanofabrication techniques. A setup was constructed that facilitates focused far-field excitation with narrow- and broadband light and detection of reflected radiation. Full polarization control of incident and reflected light was implemented. Real-space imaging and Fourier spectroscopy was used to study the photonic crystal radiation fields. Analyzed data were compared to an analytical tight-binding model.

### Sample design and FEM simulations

We used FEM simulations (COMSOL) to optimize the design parameters such that the system can offer topological protection at telecom wavelengths, with both expanded and shrunken lattices exhibiting bandgaps around 1550 nm. A fillet with a radius of 25 nm was added to the triangular corners to account for the roundedness of holes in fabrication. The periodicity of the photonic crystal was 800 nm. As indicated in fig. S4, equilateral triangles with a side of 250 nm were arranged in hexagonal clusters, with the distance from the center of cluster to the center of triangle being 243 nm for shrunken and 291 nm for the expanded lattice. Simulations were done for a 220-nm slab with a silicon refractive index of 3.48. Perfectly matched layers were added above the simulation box so that simulations of the (quasinormal) eigenmodes also yield their linewidth, which we define as two times the imaginary part of the complex eigenfrequency.

### Sample fabrication

The samples were fabricated from a silicon-on-insulator wafer with a 220-nm Si device layer on top of a 3-μm buried oxide layer, which sits on a 700-μm-thick substrate. A positive-tone electron beam (e-beam) resist, AR-P 6209, was spin-coated on top of the waferchips to form a 250-nm-thick resist layer. The photonic crystal designs were patterned in the resist using e-beam lithography (Raith Voyager, 50 kV). The resist was developed with pentyl acetate/O-xylene/MIBK(9): IPA(1)/IPA. The designed pattern was transferred into the Si device layer using HBr/O2 inductively coupled plasma etching (Oxford Instruments PlasmaPro 100 Cobra). Anisole (5 min) was used to remove the leftover resist, and the sample was cleaned using base piranha [$H_2O(5){:}NH_4OH(1){:}H_2O_2(1)$] treatment for 15 min at 75°C. To obtain freestanding photonic crystal membranes, the oxide layer was wet-etched with hydrogen fluoride, followed by critical point drying.

The main sample had an armchair-like edge with a length of ~380 μm, which separates shrunken and expanded lattices having widths of ~196 μm each. Figure S1c shows an optical micrograph of this sample. The sample used for the experiment laid out in Fig. 5 contained two armchair-like edges of ~55 μm and two zigzag-like edges of ~80 μm forming a four-way junction, separating two sets of expanded and shrunken lattices.

### Experimental details
#### Dispersion measurements

A 200-mW supercontinuum source (Fianium WhiteLase Micro) generates light with a broadband spectrum. Its output is filtered by a long pass filter with a cutoff wavelength of 1150 nm and coupled into a single-mode optical fiber. The IR light from the fiber is collimated by an achromatic lens and passed through an OD:1 neutral density filter, linear polarizer (LP), and an achromatic quarter-wave plate (QWP), which together define the polarization of the input beam. A beam splitter (BS) steers the input light to an aspheric objective (Newport 5721-C-H, 60×, numerical aperture = 0.6), which focuses light on the

sample. Reflected light is collected by the same objective and passed through the BS to the Fourier lens (FL) placed in the output path. This lens, together with a tube lens (TL), images the objective back focal plane onto the entrance slit of a spectrometer (Acton SpectraPro SP-2300i). Optional custom spatial filters (SFs) are placed in the image plane between the FL and TL to define the sample area, from which light is collected. The (vertical) entrance slit of the spectrometer, aligned with the optical axis, chooses $k_x = 0$ in the reciprocal plane, confirmed using a test grating sample. With the help of two parabolic mirrors (PMs) for focusing and collection, the spectrometer grating then disperses the broadband IR light orthogonal to the slit, such that the InGaAs IR camera (AVT Goldeye G-008 SWIR) placed at the spectrometer output records images of frequency versus $k_y/k_0$, where $k_0$ is the free-space wave vector. The spectral resolution is 81.5 GHz, and the wave vector resolution $\Delta k_y/k_0 \approx 0.011$. The wave vector axis was calibrated by observing the diffraction of a gold transmission grating with known pitch placed at the sample position. The frequency axis was calibrated using laser sources of known wavelength. Reflectometry images taken at different center frequencies of the grating are stitched together in postprocessing to plot dispersion over a wide range of frequencies.

### Polarimetry measurements

We use the "rotating QWP" scheme outlined in (38) to measure the Stokes polarization parameters. We place a QWP and LP after the FL so that the reflected beam passes through them sequentially. For a given rotation angle θ of the QWP, the detected intensity can be written in the form of a truncated Fourier series

$$I(\theta) = \frac{1}{2}(A + B\sin 2\theta + C\cos 4\theta + D\sin 4\theta) \quad (1)$$

where the Fourier coefficients $A$, $B$, $C$, and $D$ are related to the measured Stokes parameters as $S'_0 = A - C$, $S'_1 = 2C$, $S'_2 = 2D$, and $S'_3 = B$. For our polarimetry measurements, we take 12 successive measurements rotating the QWP from $\theta_1 = 0°$ to $\theta_{12} = 165°$ in steps of 15° to find these coefficients as

$$A = \frac{2}{12}\sum_{n=1}^{12}I(\theta_n), \qquad B = \frac{4}{12}\sum_{n=1}^{12}I(\theta_n)\sin 2\theta_n,$$
$$C = \frac{4}{12}\sum_{n=1}^{12}I(\theta_n)\cos 4\theta_n, \quad D = \frac{4}{12}\sum_{n=1}^{12}I(\theta_n)\sin 4\theta_n \quad (2)$$

The LP after the QWP is fixed at $0°$ with respect to the $\hat{x}$ axis in all these measurements.

The collected light is not fully polarized. The polarized component for a given output is defined as $I_P = \sqrt{{S'_1}^2 + {S'_2}^2 + {S'_3}^2}$. We normalize the measured Stokes parameters to the maximum value of the polarized component in the output as $S_i = S'_i/\max(I_p)$ for $i = 1,2,3$. Results of full polarization tomography of the edge states are given in fig. S5.

Contributions from background reflections can be important while studying the Stokes parameters of a resonant mode radiation, as the observed polarization of the superposition of both fields can depend strongly on their (uncontrollable) relative phase. We isolate the edge-mode radiation in the far field from the direct reflection components by altering the SF. Figure S6 shows a sketch of the used SFs, determining the collection area during edge-state dispersion measurements without and with a center block. With the latter, collection of direct reflections from the illumination spot is prevented, but radiation from edge states that propagate out of the center spot is detected.

### Real-space imaging

To visualize the propagation of edge modes in real space, we take out the FL, SF, and polarimetry optics in the output path. Fiber-coupled light at 1512 nm from a single-wavelength CW tunable laser (TOPTICA CTL) is delivered through the same IR fiber. The QWP and LP in the input path control polarization. In this case, the collected light is steered to a different path after the BS, and the sample is imaged onto an IR camera (AVT Goldeye P-008 SWIR) using another TL.

### Extraction of modes from dispersion cross-cut

To the normalized reflection obtained from the cross-cut in Fig. 3A, we fit a set of complex Lorentzians of the form

$$R(\omega) = \left| A_0 + \sum_{j=1}^{3} A_j e^{i\phi_j} \frac{\gamma_j}{\omega - \omega_{0j} + i\gamma_j} \right|^2 \quad (3)$$

where $A_0$ is a constant background amplitude; $A$, $\phi$, and $\omega_0 - i\gamma$ are the amplitude, phase, and complex frequency of three individual Lorentzians. Quality factors are defined as $Q_j = \omega_{0j}/(2\gamma_j)$. Two of these Lorentzians model the edge modes, while the third (broad) Lorentzian accounts for the slowly varying background reflection.

### SUPPLEMENTARY MATERIALS

### REFERENCES AND NOTES

1. C. L. Kane, E. J. Mele, Quantum spin Hall effect in graphene. *Phys. Rev. Lett.* **95**, 226801 (2005).
2. B. A. Bernevig, T. L. Hughes, S.-C. Zhang, Quantum spin Hall effect and topological phase transition in HgTe quantum wells. *Science* **314**, 1757–1761 (2006).
3. M. König, S. Wiedmann, C. Brüne, A. Roth, H. Buhmann, L. W. Molenkamp, X.-L. Qi, S.-C. Zhang, Quantum spin Hall insulator state in HgTe quantum wells. *Science* **318**, 766–770 (2007).
4. Z. Wang, Y. Chong, J. D. Joannopoulos, M. Soljačić, Observation of unidirectional backscattering-immune topological electromagnetic states. *Nature* **461**, 772–775 (2009).
5. A. B. Khanikaev, S. H. Mousavi, W.-K. Tse, M. Kargarian, A. H. MacDonald, G. Shvets, Photonic topological insulators. *Nat. Mater.* **12**, 233–239 (2013).
6. M. C. Rechtsman, J. M. Zeuner, Y. Plotnik, Y. Lumer, D. Podolsky, F. Dreisow, S. Nolte, M. Segev, A. Szameit, Photonic Floquet topological insulators. *Nature* **496**, 196–200 (2013).
7. W.-J. Chen, S.-J. Jiang, X.-D. Chen, B. Zhu, L. Zhou, J.-W. Dong, C. T. Chan, Experimental realization of photonic topological insulator in a uniaxial metacrystal waveguide. *Nat. Commun.* **5**, 5782 (2014).
8. M. Bellec, U. Kuhl, G. Montambaux, F. Mortessagne, Manipulation of edge states in microwave artificial graphene. *New J. Phys.* **16**, 113023 (2014).
9. A. P. Slobozhanyuk, A. N. Poddubny, A. E. Miroshnichenko, P. A. Belov, Y. S. Kivshar, Subwavelength topological edge states in optically resonant dielectric structures. *Phys. Rev. Lett.* **114**, 123901 (2015).
10. R. Fleury, A. B. Khanikaev, A. Alù, Floquet topological insulators for sound. *Nat. Commun.* **7**, 11744 (2016).
11. C. He, X. Ni, H. Ge, X.-C. Sun, Y.-B. Chen, M.-H. Lu, X.-P. Liu, Y.-F. Chen, Acoustic topological insulator and robust one-way sound transport. *Nat. Phys.* **12**, 1124–1129 (2016).
12. X. Cheng, C. Jouvaud, X. Ni, S. H. Mousavi, A. Z. Genack, A. B. Khanikaev, Robust reconfigurable electromagnetic pathways within a photonic topological insulator. *Nat. Mater.* **15**, 542–548 (2016).

13. M. Milićević, T. Ozawa, G. Montambaux, I. Carusotto, E. Galopin, A. Lemaître, L. Le Gratiet, I. Sagnes, J. Bloch, A. Amo, Orbital edge states in a photonic honeycomb lattice. *Phys. Rev. Lett.* **118**, 107403 (2017).

14. J. Noh, S. Huang, K. P. Chen, M. C. Rechtsman, Observation of photonic topological valley Hall edge states. *Phys. Rev. Lett.* **120**, 063902 (2018).

15. Y. Lumer, M. A. Bandres, M. Heinrich, L. J. Maczewsky, H. Herzig-Sheinfux, A. Szameit, M. Segev, Light guiding by artificial gauge fields. *Nat. Photonics* **13**, 339–345 (2019).

16. C. Brendel, V. Peano, O. Painter, F. Marquardt, Snowflake phononic topological insulator at the nanoscale. *Phys. Rev. B* **97**, 020102 (2018).

17. T. Ozawa, H. M. Price, A. Amo, N. Goldman, M. Hafezi, L. Lu, M. C. Rechtsman, D. Schuster, J. Simon, O. Zilberberg, I. Carusotto, Topological photonics. *Rev. Mod. Phys.* **91**, 015006 (2019).

18. K. Y. Bliokh, D. Smirnova, F. Nori, Quantum spin Hall effect of light. *Science* **348**, 1448–1451 (2015).

19. V. G. Sala, D. D. Solnyshkov, I. Carusotto, T. Jacqmin, A. Lemaître, H. Terças, A. Nalitov, M. Abbarchi, E. Galopin, I. Sagnes, J. Bloch, G. Malpuech, A. Amo, Spin-orbit coupling for photons and polaritons in microstructures. *Phys. Rev. X* **5**, 011034 (2015).

20. M. Hafezi, S. Mittal, J. Fan, A. Migdall, J. M. Taylor, Imaging topological edge states in silicon photonics. *Nat. Photonics* **7**, 1001–1005 (2013).

21. S. Mittal, J. Fan, S. Faez, A. Migdall, J. M. Taylor, M. Hafezi, Topologically robust transport of photons in a synthetic gauge field. *Phys. Rev. Lett.* **113**, 087403 (2014).

22. S. Mittal, E. A. Goldschmidt, M. Hafezi, A topological source of quantum light. *Nature* **561**, 502–506 (2018).

23. M. A. Bandres, S. Wittek, G. Harari, M. Parto, J. Ren, M. Segev, D. N. Christodoulides, M. Khajavikhan, Topological insulator laser: Experiments. *Science* **359**, eaar4005 (2018).

24. L. Fu, Topological crystalline insulators. *Phys. Rev. Lett.* **106**, 106802 (2011).

25. L.-H. Wu, X. Hu, Scheme for achieving a topological photonic crystal by using dielectric material. *Phys. Rev. Lett.* **114**, 223901 (2015).

26. S. Barik, H. Miyake, W. DeGottardi, E. Waks, M. Hafezi, Two-dimensionally confined topological edge states in photonic crystals. *New J. Phys.* **18**, 113013 (2016).

27. P. D. Anderson, G. Subramania, Unidirectional edge states in topological honeycomb-lattice membrane photonic crystals. *Opt. Express* **25**, 23293–23301 (2017).

28. S. Yves, R. Fleury, T. Berthelot, M. Fink, F. Lemoult, G. Lerosey, Crystalline metamaterials for topological properties at subwavelength scales. *Nat. Commun.* **8**, 16023 (2017).

29. Y. Yang, Y. F. Xu, T. Xu, H.-X. Wang, J.-H. Jiang, X. Hu, Z. H. Hang, Visualization of a unidirectional electromagnetic waveguide using topological photonic crystals made of dielectric materials. *Phys. Rev. Lett.* **120**, 217401 (2018).

30. S. Barik, A. Karasahin, C. Flower, T. Cai, H. Miyake, W. DeGottardi, M. Hafezi, E. Waks, A topological quantum optics interface. *Science* **359**, 666–668 (2018).

31. T. Ma, G. Shvets, All-Si valley-Hall photonic topological insulator. *New J. Phys.* **18**, 025012 (2016).

32. M. I. Shalaev, W. Walasik, A. Tsukernik, Y. Xu, N. M. Litchinitser, Robust topologically protected transport in photonic crystals at telecommunication wavelengths. *Nat. Nanotechnol.* **14**, 31–34 (2019).

33. X.-T. He, E.-T. Liang, J.-J. Yuan, H.-Y. Qiu, X.-D. Chen, F.-L. Zhao, J.-W. Dong, A silicon-on-insulator slab for topological valley transport. *Nat. Commun.* **10**, 872 (2019).

34. M. A. Gorlach, X. Ni, D. A. Smirnova, D. Korobkin, D. Zhirihin, A. P. Slobozhanyuk, P. A. Belov, A. Alù, A. B. Khanikaev, Far-field probing of leaky topological states in all-dielectric metasurfaces. *Nat. Commun.* **9**, 909 (2018).

35. P. St-Jean, V. Goblot, E. Galopin, A. Lemaître, T. Ozawa, L. Le Gratiet, I. Sagnes, J. Bloch, A. Amo, Lasing in topological edge states of a one-dimensional lattice. *Nat. Photonics* **11**, 651–656 (2017).

36. W. P. Su, J. R. Schrieffer, A. J. Heeger, Solitons in polyacetylene. *Phys. Rev. Lett.* **42**, 1698–1701 (1979).

37. T. H. Taminiau, S. Karaveli, N. F. van Hulst, R. Zia, Quantifying the magnetic nature of light emission. *Nat. Commun.* **3**, 979 (2012).

38. B. Schaefer, E. Collett, R. Smyth, D. Barrett, B. Fraher, Measuring the Stokes polarization parameters. *Am. J. Phys.* **75**, 163–168 (2007).

39. L. Lu, J. D. Joannopoulos, M. Soljačić, Topological photonics. *Nat. Photonics* **8**, 821–829 (2014).

40. L. Xu, H.-X. Wang, Y.-D. Xu, H.-Y. Chen, J.-H. Jiang, Accidental degeneracy in photonic bands and topological phase transitions in two-dimensional core-shell dielectric photonic crystals. *Opt. Express* **24**, 18059–18071 (2016).

41. T. Fösel, V. Peano, F. Marquardt, L lines, C points and Chern numbers: Understanding band structure topology using polarization fields. *New J. Phys.* **19**, 115013 (2017).